Energy transport analysis in ultrashort pulse laser ablation through combined molecular dynamics and Monte Carlo simulation

Wenqian Hu, Yung C. Shin, and Galen King
School of Mechanical Engineering, Purdue University, West Lafayette, Indiana 47907, USA
(Received 17 February 2010; revised manuscript received 27 July 2010; published 17 September 2010)

Mechanisms of energy transport during ultrashort laser pulses (USLPs) ablation are investigated in this paper. Nonequilibrium electron-transport, material ionization, as well as density change effects, are studied using atomistic models—the molecular dynamics (MD) and Monte Carlo (MC) methods, in addition to the previously studied laser absorption, heat conduction, and stress wave propagation. The target material is treated as consisting of two subsystems: valence-electron system and lattice system. MD method is applied to analyze the motion of atoms while MC method is applied for simulating electron dynamics and multiscattering events between particles. Early-time laser-energy absorption and redistribution as well as later-time material ablation and expansion processes are analyzed. This model is validated in terms of ablation depth, lattice/electron temperature distribution as well as evolution, and plume front velocity, through comparisons with experimental or theoretical results in literature. It is generally believed that the hydrodynamic motion of the ablated material is negligible for USLP but this study shows it is true only for its effect on laser-energy deposition. This study shows that the consideration of hydrodynamic expansion and fast density change in both electron and lattice systems is important for obtaining a reliable energy transport mechanism in the locally heated zone.

DOI: 10.1103/PhysRevB.82.094111 PACS number(s): 79.20.Eb, 52.38.Mf

I. INTRODUCTION

Ultrashort laser pulses (USLPs) material processing has been extensively studied in recent years.[1–22] This process involves multiphysical phenomena, such as optical absorption, thermal conduction, electrical field emergence, and mechanical spallation. High intensity laser heating leads to thermal stress wave propagation and material ablation. The ejected material expands in the form of clusters, droplets, or gas, either inhomogeneous or homogeneous, depending on laser fluence.[1] The detailed energy transport phenomena comprise laser-energy absorption, electron excitation, ballistic electron motion, electronic heat diffusion, photon or impact ionization, electron-phonon heat exchange, phase transition, thermal stress wave propagation, material expansion, and so on. These phenomena and their physical mechanisms are of great importance to laser micromachining and deposition. These phenomena occur on different spatial and temporal scales, on the order of 10–100 nm and 1 femtosecond (fs) ~100 picosecond (ps), respectively. Basically speaking, they all occur in a localized region and in a very short time period so the requirements of spatial and temporal resolutions for measurements of temperature, density, and pressure changes are very demanding. Therefore, USLP ablation mechanism investigation greatly depends on theoretical studies.

In metals, laser energy is absorbed predominantly by nearly-free electrons through inverse Bremsstrahlung; however, in semiconductors/insulators, the nearly-free electrons have to be generated first through photon ionization and avalanche ionization. The energy is then transferred to the lattice through electron-phonon coupling, which takes a longer time than the electron excitation process. Therefore, the material being ablated can be treated as a two-temperature system. Parabolic two-temperature model (TTM) (Ref. 2) is generally used for pulses below 10 ps but above 100 fs because it does not account for laser-plasma/plume interaction and assumes thermal equilibrium in the electron system for all time. For pulses below 100 fs, hyperbolic TTM,[3,4] in which electron nonthermalization is considered, has been used. TTM essentially solves a one-dimensional heat conduction problem and are valid only when the laser spot diameter is much larger than the optical or thermal penetration depth. Nevertheless, this type of model is widely used because of its simplicity and acceptable accuracy in describing energy transport mechanism inside the solid target.[5–8] Semiclassical TTM has been proposed to include the effects of nonequilibrium electron transport and electron drifting.[9]

Due to the energy transfer from the electron system, the lattice system is heated up to a high temperature, which is on the order of its critical temperature. This heating process is almost isochoric so a strong compression stress wave is generated inside the material. Afterward, the material undergoes structural modification and density change, where hydrodynamic motion starts to take place. Common hydrodynamic models describe the evolution of the electron, ion, and radiation fields, with considerations of conservations of mass, momentum, and energy on the continuum level while some of these models incorporate TTM into the hydrodynamic equations.[10–15] Each field of electron, ion, and radiation is treated individually in a fluid approximation and assumed to be in local thermodynamic equilibrium.[13] This type of model has been applied to laser ablation simulation for femtosecond, picosecond, and nanosecond pulses, with the inclusion of laser-plasma interaction.

However, highly nonequilibrium states and fast phase transformations induced by USLP irradiation cannot be reliably described by continuum models.[16] These phenomena have to be described by atomistic models, such as the molecular dynamics (MD) method. MD simulation provides an explicit atomistic representation of material structure change, e.g., melting, vaporization, spallation, and expansion. The

material structure change is a nonthermal channel of energy redistribution but it can have an important effect on the kinetics of thermal and mechanical relaxation of the lattice, which is accounted for in the hybrid TTM-MD model but not in the conventional TTM.[16]

The electron transport has been dealt with in several implicit ways in order to be coupled with MD: the laser energy is deposited along the electron thermal diffusion length and the atoms are excited correspondingly,[17] or the electron energy is analyzed using TTM while the atoms are subjected to an external force[18] or the atoms' velocities are scaled up due to electron-phonon coupling.[19] In addition to the coupling, more complicated electron dynamics occurs during laser ablation. The ballistic electron motion and photoionization or impact ionization have significant effects on energy transport mechanisms and are not negligible. Besides, the density change in the material affects the electron heat diffusion a lot. The first work considering nonequilibrium conduction electron distributions, excitation, and ionization for laser-dielectrics interaction is done by Stuart *et al.*[20] These electron transport mechanisms have been simulated using a Monte Carlo (MC) method for laser-semiconductor interaction.[21] The MC method has also been used to study electron transport in conductors with Pauli exclusion principle accounted for through self-scattering and scattering rates determined by perturbation theory in quantum mechanics.[23] Electron transport can also be solved by using Boltzmann transport equation for metals, semiconductors, and insulators.[22]

This paper presents a combined MD and MC method to associate atom motions with multiscattering events, and thus to investigate a more comprehensive particle transport and energy transport mechanisms during USLP ablation of metals. The MC method is used to simulate electron dynamics, not only thermal diffusion but also electron excitation and ionization. The effect of material structure change is also considered. This combined MD-MC model is different with the one of Ref. 21 because the laser-energy absorption mechanisms of the target materials (metals in this study, semiconductors in Ref. 21), as well as the handling of energy coupling between lattice and electron systems, are different. In the following paragraphs, basic physical mechanisms are first discussed and followed by the simulation methods and results.

II. PHYSICAL MECHANISMS

Basic mechanisms during laser ablation of metals in vacuum include photon absorptions (e.g., via collisions by the inverse bremsstrahlung effect), electron-phonon collisions, electron-electron collisions, excitations/deexcitations and ionizations/recombinations, as well as atom and ion evolutions. Recombination is not considered in this study because it occurs on a long time scale of nanosecond. For metals, their outermost electrons are loosely bound and essentially free to travel among atoms, and thus called nearly-free electrons. At the very beginning of laser pulse irradiation, the nearly-free electrons are excited from a lower energy state to a higher state due to photon absorption during collisions with atoms.[24] This excitation processes can be applied not only to the electron at the initial state before laser irradiation but also excited states.[25] At this time, electrons are in high nonequilibrium and ballistic electron motions dominate.[26] Ballistic electrons are first generated and concentrated in the skin layer, the region where laser energy is absorbed most, and then propagate with great kinetic energy without collision in a long mean-free path. Ballistic electron motion extends the absorption depth beyond the skin depth (in the order of 10 nm), which is especially significant for noble metals, to about 100 nm.[26] Ballistic electrons that propagate toward the metal surface may have enough kinetic energy (larger than the work function) and escape from the metal surface; otherwise they are drawn back by the confining potential at the metal-vacuum interface.[27] The ballistic electrons eventually will undergo electron-electron scattering with its own characteristic collision time τ_{ee}. After electrons have reached thermal equilibrium through scattering, they are relaxed by collisions with phonons.

During the photon absorption process mentioned above, electron excitation and ionization may occur, the latter of which is a limited case of the former. To understand the ionization process, it is important to distinguish nearly-free electrons and free electrons of metals. The nearly-free electrons travel among atoms within the material but they need to obtain sufficient energy in order to be totally free and leave the material. The generation of free electrons is the ionization process. Single-photon ionization is a characteristic of only the UV laser pulse while multiphoton ionization (MPI) is dominant for longer wavelengths. The definition of multiphoton ionization of metal is varied in different literatures. One definition is the process where the outermost (nearly-free) electrons or bounded electrons absorb several photons simultaneously or continuously and leave the material eventually. This type of process has been observed through several independent measurements.[28–31] The laser peak power intensities utilized in these investigations are in the range of 10^9-10^{14} W/cm^2 and ionization of bounded electrons needs much higher intensities[32] so this MPI process removes only outermost electrons. The other definition of MPI is limited to bounded electron ionization where the photon absorptions have to occur within a very short time (a few femtoseconds) in order to excite the bounded electrons to a stable state, similar to that of semiconductors.[32,33] Very high intensity laser ablation is not the subject of this study so only the outermost electron excitation/ionization is considered and the first definition is adopted. After free electrons are generated, electron impact ionizations can also occur, where more free electrons will be generated during collisions between atoms and free electrons [inelastic collisions involving two or more heavy particles are negligible due to much smaller cross sections at temperature below 10 eV (Ref. 25)].

It should be noted that the free electron is different from the ballistic electron. The former is not bound to the material while the latter is due to the work function. They are both generated primarily in the skin layer but then the free electron will leave the material within a very short time while the ballistic electron is most likely to stay within the material, which makes the collision between these two types of electrons almost impossible because of the long mean-free path

of the ballistic electron. The emission of free electrons contributes to the surface electrostatic field. It is interesting to note that the electrostatic field can be very strong and beams of protons have been observed with ultraintense laser.[34]

Due to the energy exchange with electrons via electron-phonon coupling, the lattice is heated up and a compressive stress wave propagates into the material. The relaxation of this wave leads to the expansion of the material and the generation of a tensile stress wave following the compressive stress wave. For thin films, the compressive wave is reflected at the rear side of films and generates another tensile stress wave that may superimpose on the former tensile stress wave.[35] In other words, the superposition of those thermal stress waves generates a directional reversal of stress field, from compression into tensile.[36] This tensile stress causes material spallation at the central region of the film and creates only one spallation zone. For thicker films, both the front layer ablation and rear-side spallation occur.[37,38] The major driving force of the front layer ablation is the strong tensile stress in the rarefaction wave (discontinuity region of the stress wave) while the electron blast force first predicted as significant[39] is found to have little effect later on.[36] The spallation mechanism of the thicker films is the same as that of the thin films, except that it occurs near the rear side. For bulk material, the compressive wave's energy dissipates as it moves to the rear side and thus only front layer ablation occurs. In the locally heated zone, material layers undergo significant pressure, temperature, and density changes. Some material layers will go across the binodal curve or above, in inhomogeneous or homogeneous states, depending on laser fluence.

III. SIMULATION METHODS

A. Material and simulation domain

The target material of choice is fcc metal, such as Cu, Au, and Ni but not limited to those. Ni is transition metal and Au is noble metal while Cu can be taken as transition metal and noble metal. Cu has a larger electron-phonon coupling constant than Au and Ni. On the other hand, Cu and Au have much higher thermal conductivities than Ni. These materials with different properties are intentionally chosen in order to check the applicability and generality of this model.

Taking into consideration both of the statistical stability and computational cost, the simulation domain is selected to have 1200 monolayers (MLs) with 72 atoms per ML, with the dimension of several square nanometers in the horizontal plane xy and hundreds of nanometers in vertical direction z, as shown in Fig. 1. An MD method is applied to analyze the motion of atoms while an MC method is applied for simulating electron dynamics and multiscattering events between particles. The actual domain is a laser-drilled microhole with diameter on the order of 10 μm and depth on the order of 10 nm. With this aspect ratio of 1000:1, the lateral periodic boundary conditions (PBCs) can be applied. The PBC should not be applied when there are significant variations along the radial direction. It takes about 160 h for 16 processors (2.33 GHz) running in parallel to finish the simulation of 1 ns time period.

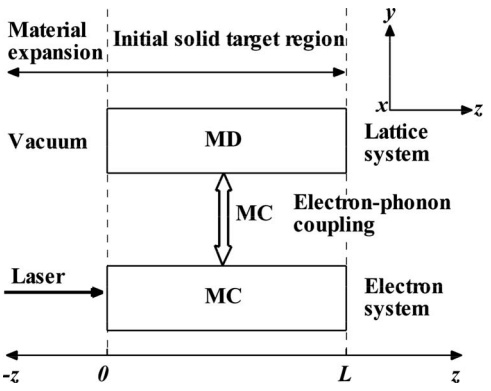

FIG. 1. Schematics of the simulation domain and approaches. Lattice system is simulated using MD method while electron dynamics and multiple-particle scattering events are simulated using MC method.

B. Atom dynamics

The initial atom positions are generated by a lattice dynamics software GULP, according to the space group of the target material. Morse pair potential, instead of many-body potentials, is used in this study to reduce computation time. It is shown that simulations using Morse potential can predict metal pressure-volume dependence and specific heat very accurately while elastic constant and bulk modulus can be predicted fairly well.[40–42] Its effect on thermoelastic stress will be discussed in the next section. For laser ablation, Morse potential has been verified its validity through comparisons of ablation depth with experimental values.[1,17,40] The atom system is equilibrated at 300 K using the dissipative particle dynamics (DPD) method[43] and let run for 1 ns without external force to check the equilibrium stability. After initial temperature equilibrium is reached, nonequilibrium molecular dynamics ensembles are used to simulate the atom dynamics including energy exchange with electrons. The atom motion is governed by the intermolecular potential and the electron-phonon coupling. The equation of motion for atom i is[18]

$$M\frac{d^2\vec{r}_i}{dt^2} = -\nabla_{\vec{r}_i}V - \frac{g}{C_l}\frac{T_l - T_e}{T_l}M\vec{v}_i^*, \tag{1}$$

where M is the atom mass, $\vec{r}_i$ is the position of atom i, $-\nabla_{\vec{r}_i}V$ is the force calculated from the intermolecular potential, g is the electron-phonon coupling factor, T_e is the electron temperature and T_l lattice temperature, C_l is the lattice specific heat, and $\vec{v}_i^* \equiv \vec{v}_i - \vec{v}_c$ is the thermal velocity, the difference between the actual velocity and the center of mass velocity. The simulation domain is divided into layers of thickness equal to the cut-off radius. The macroscopic properties, such as T_e and T_l, are calculated in each layer. Electrons and atoms exchange energy within these layers, and the atom velocity is scaled up using the electron-phonon coupling term, which is proportional to the temperature difference $T_e - T_l$. It should be noted that the coupling term scales the atom thermal velocity, not the actual velocity, and thus this equation of motion is momentum conserving (see the Appendix).[44] The effect of this energy exchange on electron dynamics is con-

sidered, which will be explained in the next section. Verlet velocity scheme is used to solve the equation of motion.[45] During the simulation of laser ablation, the time step Δt even at 5 fs is shown to be adequate through a time-step sensitivity analysis. For the boundary conditions of simulation domain, a free boundary is set at the top, lateral directions are set to be periodic, and the nonreflecting boundary condition is applied at the bottom.[18]

C. Electron dynamics and multiscattering events

As mentioned in Sec. II, very high intensity laser ablation and bounded electron excitation are not considered in this study. The subject of this study is valence-electron dynamics and relevant scattering processes. For the energy distribution, the quantum Fermi-Dirac statistics should be used if the target studied is at low temperatures (e.g., room temperature) or high concentrations (e.g., white dwarf) while the Maxwell-Boltzmann statistics can be used as an approximation at high temperatures while concentrations are not extremely high.[24] In this study, the electron system at temperatures over several electron volt (eV) is of interest, and thus this approximation is valid. Therefore, the valence electron system is treated as the Drude classical electron gas, whose energy follows the Maxwell-Boltzmann distribution function at equilibrium. Each valence electron is initially assigned with position $\boldsymbol{r}_{ei}$, velocity $\boldsymbol{v}_{ei}$, and kinetic energy $\varepsilon_{ei}=m_e\boldsymbol{v}_{ei}^2/2$. The initial distributions of electrons are random, and then redistributed to reach equilibrium by using the Metropolis method with the long-range Coulomb potential.[45]

The Monte Carlo method is extensively used for simulations of semiconductor carrier transport,[21,46] high-energy electron transport in metals,[47,48] and plasma particle transport,[49] where the Maxwell-Boltzmann distribution is applicable. As mentioned above, the Drude classical electron gas model is used in this study and the Maxwell-Boltzmann distribution is applicable so the application of MC method is valid. In this study, the MC method is used to simulate the photon absorption process and the scattering processes.

To simulate the electron absorption of photons, the simulation domain is divided into layers with a thickness smaller than 1 nm in the z direction. The electrons in each layer have an equal probability to absorb a photon. The photons are distributed following Lambert-Beer's law, i.e., with a cumulative probability decreasing exponentially with depth,[18]

$$S=(1-R)\alpha I\exp(-\alpha z), \tag{2}$$

where I is the laser power density reaching the target surface, temporally Gaussian while assumed to be spatially flat top, α is the absorption coefficient, and R is the surface reflectivity. Photons are distributed randomly in the horizontal plane.

The scattering processes include electron-electron/electron-phonon scatterings and impact ionization. The total scattering rate is defined as,[21,46]

$$\Gamma_0=1/\tau_0\geq\Gamma_{real}(\varepsilon_{ei})+\Gamma_{self}(\varepsilon_{ei})=\Sigma\Gamma_j(\varepsilon_{ei})=\Sigma 1/\tau_j(\varepsilon_{ei}), \tag{3}$$

where $\Gamma_{real}(\varepsilon_{ei})$ is the real instantaneous collisional rate, $\Gamma_{self}(\varepsilon_{ei})$ is the self-scattering rate, and $\Gamma_j(\varepsilon_{ei})$ is the individual probable physical scattering mechanism characterized by a collision time τ_j. The self-scattering mechanism is defined such that the final state before and after scattering is identical and has no effect on the momentum and trajectory of the electron, the introduction of which, however, makes the total scattering rate constant.[46] The time step of the MC method is thus $\Delta t=\tau_0$. It should be noted that this time step may have to be smaller than that of the MD method, in which case one-step MD running should be coupled with multiple-step MC running. The specific scattering mechanism $\Gamma_j(\varepsilon_{ei})$ is chosen with probability τ_0/τ_j for each electron, and this event may instantaneously change the kinetic energy and velocity of the electron but not its position.

For the energy exchange during each collision event, a simplified scheme is used to approximate each individual electron pair collision to be the collision between an electron and an energy-resolved electron fluid. This scheme is valid provided that quasineutrality holds over dimensions much greater than the Debye length.[50] During electron-electron scattering, the energy change for each electron is[50,51]

$$\begin{aligned}&\Delta\varepsilon_1=-\varepsilon_1\varsigma,\quad \Delta\varepsilon_2=+\varepsilon_1\varsigma,\quad \text{if}\quad \varepsilon_1\geq\varepsilon_2,\\ &\Delta\varepsilon_1=+\varepsilon_2\varsigma,\quad \Delta\varepsilon_2=-\varepsilon_2\varsigma,\quad \text{if}\quad \varepsilon_1<\varepsilon_2,\end{aligned} \tag{4}$$

where ε_1 and ε_2 are the original kinetic energy of these two electrons, ζ is a random number between 0 and 1. This scheme conserves kinetic energy and thus satisfies the energy conservation law because the potential energies of the electrons are not changed. The electron momentum may not always be conserved in a specific collision event but it is conserved as a whole because the direction of the electron velocity after collision is randomly chosen.

Electron-phonon scattering is dealt with as a virtual phonon exchange process[52,53] between two electrons, and in the meanwhile the electron system transfers energy to the lattice system according to the coupling term in Eq. (1). For each layer mentioned in Sec. III B, the amount of transferred energy is calculated per MD time step, and electrons that will experience the electron-phonon scattering in this MD time step share this amount of energy. The energy is thus conserved using this method because the amount of energy added to (or deducted from) the lattice system is exactly the same as that deducted from (or added to) the electron system.

For impact ionization, the original kinetic energy of the impact electron ε_{imp} split into the ionization energy ε^{ion} and the total kinetic energies of the impact electron and generated electron ε_{new},[51]

$$\Delta\varepsilon_{imp}=-\varepsilon^{ion}-(\varepsilon_{imp}-\varepsilon^{ion})\varsigma,\quad \Delta\varepsilon_{new}=+(\varepsilon_{imp}-\varepsilon^{ion})\varsigma. \tag{5}$$

The reverse process corresponds to recombination.

The aforementioned energy exchange scheme drives the electron system energy distribution to be Maxwellian, which corresponds to the classical electron gas model. It should be noted that the phenomenon that a few ballistic electrons can escape from the metal surface (as mentioned in Sec. II) is neglected and all ballistic electrons are confined in the metal during simulation. The energy transport between free

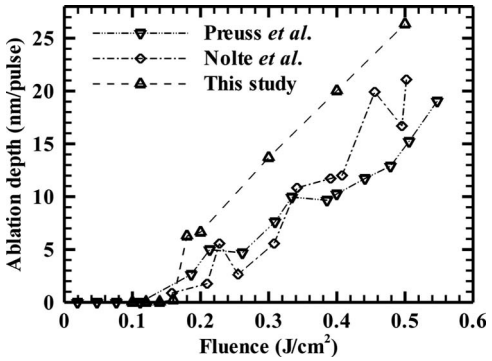

FIG. 2. Dependence of ablation depth on fluence for 0.5 ps laser irradiation of Cu. ▽: experiments by Preuss *et al.* in Ref. 57, at a wavelength of 248 nm. ◇: experiments by Nolte *et al.* in Ref. 58, at a wavelength of 780 nm. △: simulation results obtained in this study, at a wavelength of 248 nm. Curves connecting symbols are drawn only for the guide of the eyes.

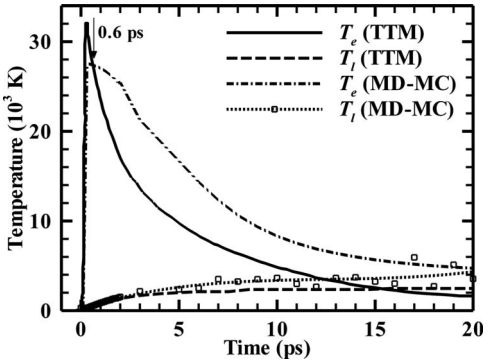

FIG. 3. Time history of electron temperature T_e and lattice temperature T_l at the front surface of the material with comparisons with results obtained by a TTM in Ref. 9. Laser pulse duration: 100 fs; wavelength: 630 nm; absorbed laser fluence: 0.1 J/cm^2. Material: Au.

electron/ions and valence electrons/lattice are neglected based on the assumption that the early plasma will expand with a great velocity from the material. Interaction between the ablated material and the laser pulse is also neglected for the USLP regime.[54]

IV. RESULTS AND DISCUSSION

Simulation results are presented in this section in terms of ablation depth, electron/lattice temperature, and plume front velocity. The initial front surfaces of the ablation targets in the following discussions are all located at the origin of the horizontal coordinate axis, as shown in the graphs. Material property parameters used in the simulations, such as reflectance, absorption coefficient, and particle collision rates (or corresponding cross sections), some of which are temperature dependent, are taken from Refs. 6, 18, 19, 55, and 56. Several results are compared with literatures. The parameters used in this study are chosen to be the same (if possible) as in these literatures, and thus the difference in results will be primarily due to different mechanisms applied in the models. This model has no free adjustable parameters.

A. Ablation threshold and rate

The dependence of ablation depth of Cu on fluence has been studied against the experimental data available in a couple of references.[57,58] The simulation results of 500 fs, 248 nm laser ablation generated by this combined MD-MC model are compared with these experimental results in Fig. 2, and match fairly well. The ablation threshold calculated in this study is 0.18 J/cm^2, similar to the experimental values of 0.17 J/cm^2 for 500 fs laser at 248 nm (Ref. 57) and 0.14 J/cm^2 for 150 fs laser at 780 nm.[58] The ablation threshold is defined in the simulation when a significant number of atoms are removed from the material. It is easy to distinguish melting, vaporization, and ablation using this atomistic model. In the melting process, atoms first experience expansion and then return to the substrate as the material cools down. In the vaporization process, a small amount of atoms leave the material with a temperature slightly above the boiling point. Vaporization occurs at a laser fluence of 0.16 J/cm^2, as predicted by this MD-MC model with a material removal depth of 0.221 nm. The material removal depth increases sharply to 6.268 nm when laser fluence is increased to 0.18 J/cm^2, where many atoms expand away from the surface in a collective motion and thus ablation occurs. The ablation threshold predicted in this study matches well with the experimental values, which justifies the application of Morse potential even though it cannot predict the thermoelastic properties very accurately.

The ablation depth simulated by the combined MD-MC model increases almost linearly after the ablation threshold in this fluence range (0.2–0.5 J/cm^2). The simulated ablation depth is for a single-pulse ablation while the experimentally obtained ablation depth is the average value of multiple-pulse ablation. Comparing multiple-pulse ablation with single-pulse ablation, more laser energy is reflected away from the preformed crater than from a fresh flat surface, and it is more difficult for the material inside the deeper crater to expand and flow away so the averaged ablation depth is lower than the single-pulse ablation depth. Therefore, the overall simulated ablation depths are a little larger than the experimental values.

B. Energy absorption and redistribution at early times

1. Ballistic electron motion, ionization, and heat conduction

During the first several or tens of picoseconds, the laser energy absorbed by the electron system is gradually transferred to the lattice system. The temporal evolutions of electron temperature T_e and lattice temperature T_l of the front surface material layers of Au, ablated by 100 fs, 630 nm laser, are shown in Fig. 3. Due to the effects of ballistic electron motion and ionization considered in this study, a portion of energy propagates into the deep material and a portion of energy is exhausted during the ionization so T_e is a little lower during the first 0.6 ps as compared with the data predicted by the TTM. As ballistic electron motion ceases, common electron heat conduction takes place but the heat

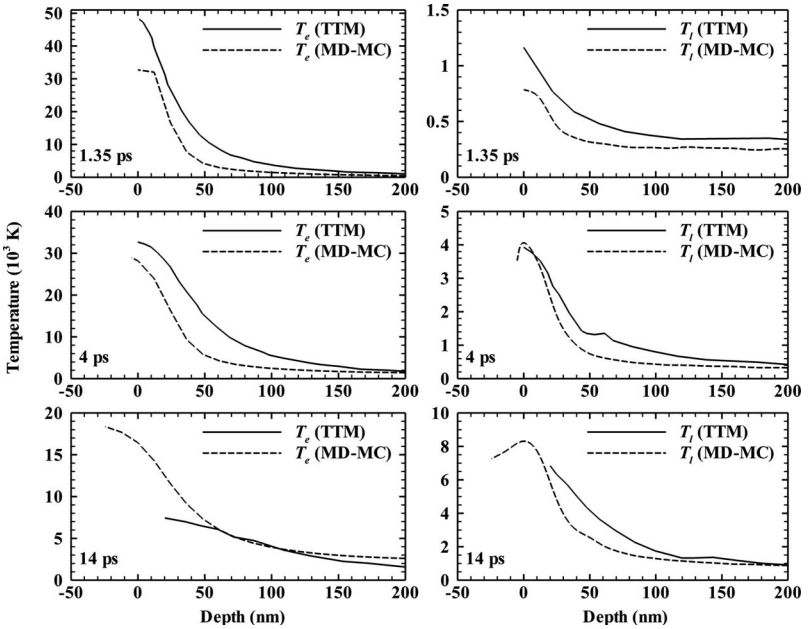

FIG. 4. Temperature distribution of electron temperature T_e (left) and lattice temperature T_l (right) with comparison with results obtained by a TTM in Ref. 5 at 1.35, 4, and 14 ps. Laser pulse duration: 500 fs; wavelength: 248 nm; absorbed laser fluence: 0.2 J/cm^2. Material: Au.

conduction rate is very low compared with that of a room-temperature solid. The electron thermal conductivity is not only determined by the electron temperature but also affected by the lattice structure. As the lattice structure becomes disordered, the heat conduction is decreased similarly to what occurs during the metal-dielectric transition.[59] Considering these effects, after 0.6 ps, T_e predicted by the MD-MC model is higher than the TTM result that neglects this lattice structure effect since the thermal conduction from the surface material to the deep material is reduced more significantly. This phenomenon also leads to a higher lattice temperature T_l at the surface. The lattice temperature simulated by the MD-MC model demonstrates some oscillations after 10 ps as the material goes through significant structure change. The application of the Morse pair potential may also cause surface temperature oscillations because the Morse potential works fine for structures inside a bulk material but may not work well at the surface due to decreased coordination, especially for Au.[60]

The results imply that the electron-lattice coupling occurs at the time around 20 ps, which is a little longer than 15 ps predicted by the TTM. This coupling time is determined primarily by the electron-lattice coupling constant of the material, i.e., Au has a smaller coupling constant than Cu so the coupling time for Au will be longer than Cu generally. This coupling time is also affected by the difference between electron temperature and lattice temperature of the laser-ablated zone; if this difference is larger, the coupling time will be longer.

2. Solid-liquid phase change

For the spatial distributions of electron temperature T_e and lattice temperature T_l of Au target at different times (Fig. 4), a resemblance to the trend obtained by a TTM in Ref. 5 is found for material at or below the initial surface. The laser used is a 500 fs laser at 248 nm with an absorbed fluence of 0.2 J/cm^2. For the material beyond the initial surface, comparison cannot be made because a confined domain is used in Ref. 5 with the application of TTM.

At 1.35 ps, T_e and T_l calculated by the MD-MC model are lower than those calculated by the TTM, due to the effects of ballistic electron motion and ionization mentioned above. At 4 ps, T_e is still lower but the maximum lattice temperature calculated by MD-MC model is a little higher than that calculated by the TTM. To analyze this phenomenon, the number density and the mass density of the material are calcu-

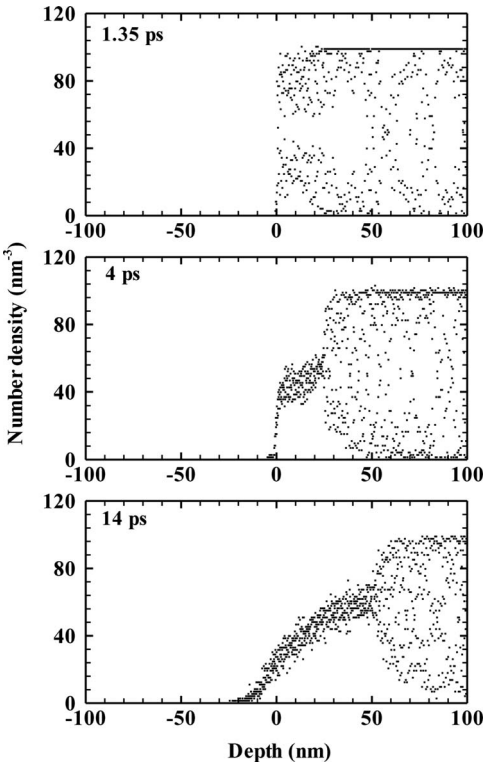

FIG. 5. Number density evolution of the lattice system. Laser and material parameters are the same as in Fig. 4.

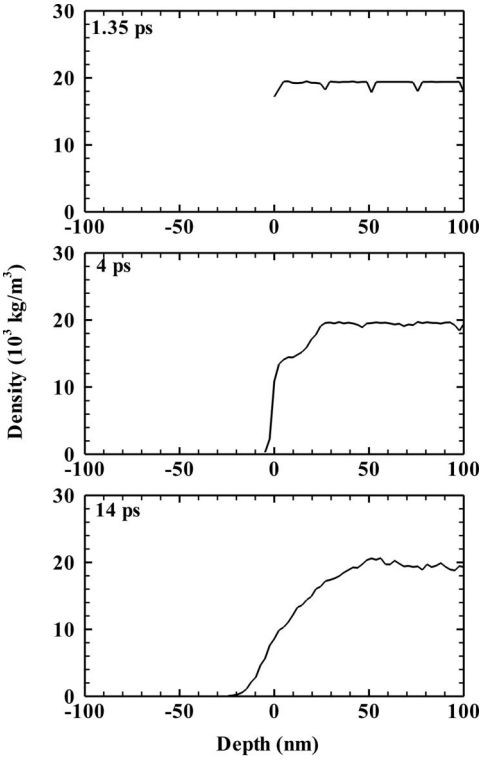

FIG. 6. Mass density evolution of the lattice system. Laser and material parameters are the same as in Fig. 4.

lated and shown in Figs. 5 and 6, respectively. The number density distribution shows that the material structure of the top layer (in the range of 0–20 nm) is not intact anymore at 1.35 ps but its mass density does not change much. Then this layer becomes liquid at 4 ps and the mass density of the material at the surface drops a lot. This huge density change plays a significant role in the laser-energy redistribution and material temperature change. The following hydrodynamic equation is derived from the one in Ref. 10:

$$\left(\frac{\partial U_l}{\partial T_l}\right)_\rho \frac{dT_l}{dt} + \left[\left(\frac{\partial U_l}{\partial \rho}\right)_{T_l} - \frac{p_l}{\rho^2}\right]\frac{d\rho}{dt} = K_{e\text{-}l} - H_l, \qquad (6)$$

where U_l is the lattice internal energy per unit mass, p_l is the lattice pressure, ρ is the mass density per unit volume, $K_{e\text{-}l}$ is the energy exchange rate between electrons and the lattice, and H_l is the latent heat absorption rate during phase change when it is applicable. The fusion latent heat is one or two orders of magnitude smaller than the electron-lattice energy exchange. During the time period from 1.35 to 4 ps, the material temperature increases from 0.8×10^3 to 4×10^3 K, and mass density changes from 19×10^3 to 14×10^3 kg/m^3 (an average value of the material in the range of 0–20 nm). QEOS (quotidian equation of state, Ref. 61) data are used to calculate and compare the influence of the two terms on the left-hand side of the equation, and it is found that the first and the second terms are on the same order but have different signs. The effect of the $\frac{d\rho}{dt}$ term is not considered in the TTM. Therefore, even the source term is lower for the MD-MC case, the maximum lattice temperature is higher than that calculated using the TTM.

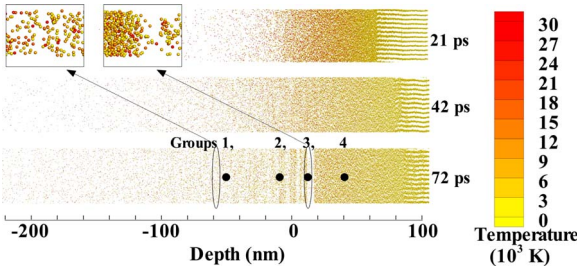

FIG. 7. (Color online) Material structures evolution. Laser pulse duration: 100 fs; wavelength: 248 nm; absorbed laser fluence: 1.0 J/cm^2. Material: Ni.

The effect of density change is more significant at 14 ps shown in Fig. 4. The MD-MC model predicts much higher T_e than the TTM value for the portion of the material that has experienced the phase change and density change (depth within 50 nm, see Figs. 5 and 6) while T_e within the solid region of the material (depth above 50 nm) matches well with the TTM value. The differences arise primarily because the current MD-MC model takes into account the hydrodynamic motion and fast density change in the ablated material, not only for the lattice system, which is naturally included by using MD, but also for the electron system that dominates the heat conduction rate. As discussed before, TTM essentially solves the heat conduction problem inside the solid target. The hydrodynamic equation for the electron system is given by[10]

$$\left(\frac{\partial U_e}{\partial T_e}\right)_\rho \frac{dT_e}{dt} + \left[\left(\frac{\partial U_e}{\partial \rho}\right)_{T_e} - \frac{p_e}{\rho^2}\right]\frac{d\rho}{dt} = H_e + X_e + K_{e\text{-}l}, \quad (7)$$

where U_e and p_e are electron internal energy per unit mass and pressure, respectively, H_e is the electron heat conduction term, and X_e is the laser-energy absorption rate. Even if the material property dependence on the density can be included and described by the first term on the left-hand side of Eq. (7), a major contribution due to the effect of the density change with time is neglected in TTM since the second term is neglected. It is verified that the term $[(\frac{\partial U_e}{\partial \rho})_{T_e} - \frac{p_e}{\rho^2}]$ is positive by using the QEOS table[61] generated near the solid density (50–100 %) and around tens of thousand degrees. Therefore, the second term $[(\frac{\partial U_e}{\partial \rho})_{T_e} - \frac{p_e}{\rho^2}]\frac{d\rho}{dt}$ is always negative because the term $\frac{d\rho}{dt}$ is generally negative (some exceptions will be explained in the next section) during material expansion. As a result, the electron temperature of the expanded plume is underestimated when using TTM, which is also true for the lattice temperature because electron and lattice systems are already in equilibrium at this time.

C. Material ablation and plume expansion at later times

The material structures of Ni during USLP laser ablation are plotted in Figs. 7 and 8. It should be noted that the horizontal and vertical scales of these figures have a very small ratio, 1:20. Therefore, the cluster interfaces may

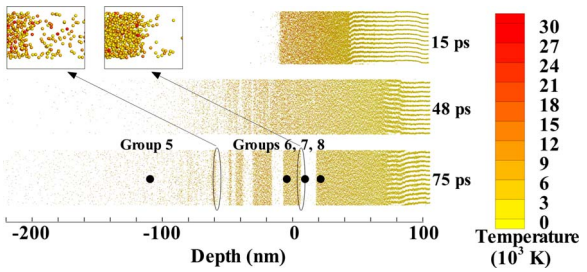

FIG. 8. (Color online) Material structures evolution. Laser pulse duration: 100 fs; wavelength: 248 nm; absorbed laser fluence: 0.27 J/cm^2. Material: Ni.

falsely look sharp. Closeup views with 1:1 ratio are included to Figs. 7 and 8 to show the details. Corresponding number density evolutions and lattice temperature developments are shown in Figs. 9–12. Several groups of atoms are chosen from Figs. 7 and 8 and their thermodynamic trajectories are plotted in Figs. 13 and 14.

1. Liquid-vapor phase change

For the ablation at a moderate fluence (1.0 J/cm^2, absorbed), Figs. 7 and 9 show that at 21 ps the material layers at depths around −20–60 nm have a liquid-vapor mixture structure, and the number density is not uniform. The material layers above −20 nm are in the vapor state with very low and uniform number densities. At later times (42 and 72 ps), more liquid layers transform into vapor, and vapor layers and liquid layers are separated at 72 ps. The density evolution process is different at a lower laser fluence (0.27 J/cm^2, absorbed), as shown in Figs. 8 and 10. A larger portion of the material layers remain solid throughout the ablation process. At 75 ps, several dense regions (liquid or liquid-vapor mixture) at depths around −40–0 nm are separated by vapor layers, which represent the occurrence of spallation (reasons will be explained in the next section). At this fluence level (a few tens of joule per square centimeter), similar characteristics of liquid-vapor phase transition are explained in Ref. 62 using an analytical model.

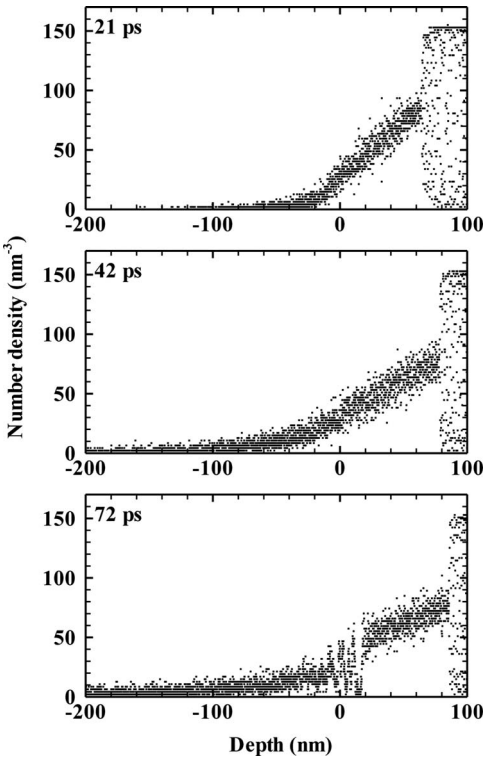

FIG. 9. Number density evolution of the lattice system. Laser and material parameters are the same as in Fig. 7.

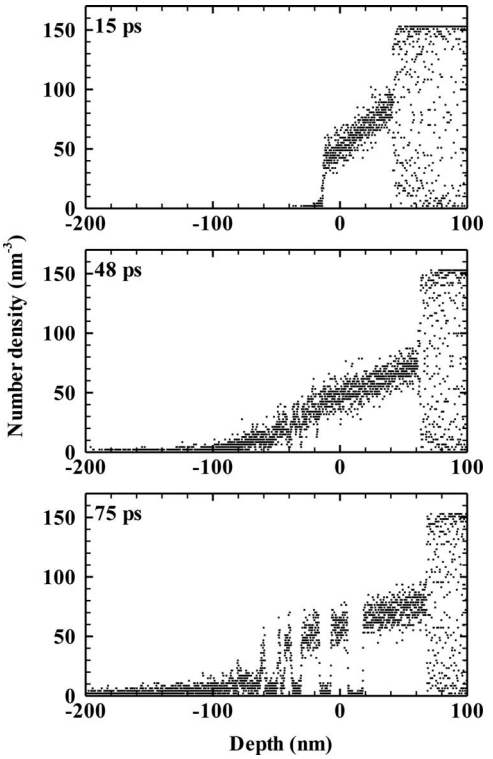

FIG. 10. Number density evolution of the lattice system. Laser and material parameters are the same as in Fig. 8.

The lattice temperature developments are compared with the results obtained by a TTM-MD model in Ref. 19 (Figs. 11 and 12). Similar trends of temperature distribution are found for material below the initial surface where liquid-vapor phase change has not occurred. However, the behaviors of ejected material which moves away from the initial surface are very different. When a moderate fluence is applied (1.0 J/cm^2, absorbed), the ablated material expands in a comparatively homogeneous state (Fig. 9) and the plume temperature obtained in this study is higher as explained in Sec. IV B 2. It should be noted that the simulation domain depth is in the range of −250 to 200 nm when analyzing the results shown in these figures. Moreover, the material temperature predicted by the MD-MC model shows some oscillations in the vapor region due to the decreased atom number density. When a lower laser fluence (0.27 J/cm^2, absorbed) is used, different plume front velocities are found (Fig. 12). At 15 ps, the material state is still close to homogeneous (Fig. 10), and thus Eqs. (6) and (7) can be used to explain the difference of plume temperature shown in Fig. 12. After that, liquid-vapor phase change occurs and large density oscillations lead to a significant discrepancy in plume front veloci-

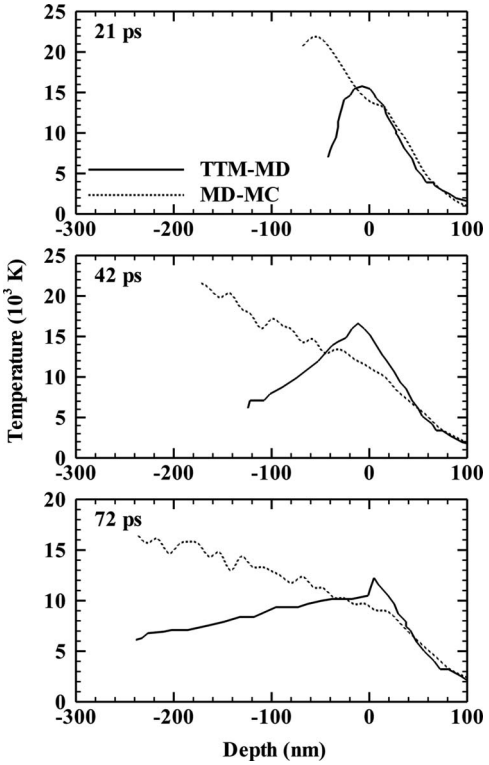

FIG. 11. Temperature distribution in the lattice system with comparison with results obtained by a hybrid TTM-MD model in Ref. 19 at 21, 42, and 72 ps. Laser and material parameters are the same as in Fig. 7.

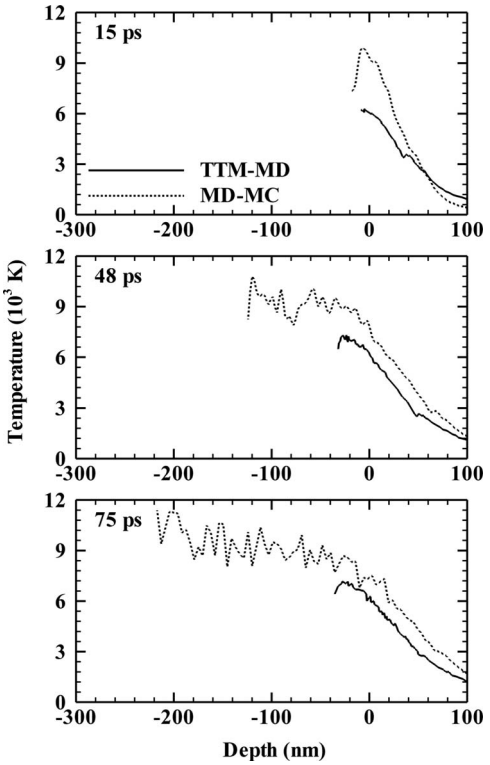

FIG. 12. Temperature distribution in the lattice system with comparison with results obtained by a hybrid TTM-MD model in Ref. 19 at 15, 48, and 75 ps. Laser and material parameters are the same as in Fig. 8.

ties, as shown at 48 and 75 ps in Fig. 12. The expansion of these ablated clusters has been observed to be very quick (on the order of 1 km/s) in this study, seemingly a little higher than what is obtained in experiments at this low fluence. But the experimentally obtained expansion velocity is usually at a delay time of nanoseconds, which should be lower than the expansion velocity in the first 100 ps.

2. Thermodynamic trajectories and ablation mechanisms

To reveal how material layers undergo phase change from solid to vapor, thermodynamic trajectories of eight atom groups are plotted on a temperature-density diagram in Figs. 13 and 14. The data of the critical point, the binodal and the spinodal are obtained from Ref. 19. The locations of the atom groups at 72 or 75 ps are labeled in Figs. 7 and 8, respectively. If the atom groups are chosen at 0 ps, the thermodynamic trajectory of each atom can be very different, becoming evaporated or condensed back finally, even if they are at the same depth at 0 ps. Groups 1–4 are chosen for the moderate fluence while groups 5–8 are chosen for the low fluence. Groups 2–4 and 6–8 are around the material separation zone, and groups 1 and 5 are in the front part of the plume. Their initial depths of those atom groups in the target are shown in Figs. 13 and 14. The numbers along with each thermodynamic trajectory are the time delays (unit: ps) corresponding to specific temperature and density states. At each fluence, the group of atoms which are initially located deeper has a lower overall temperature and is slower in the phase change progress as well.

For the moderate fluence, the thermodynamic trajectories of atom groups 1 and 2 go smoothly across the temperature-density diagram, where the density keeps decreasing while the temperature jumps at the beginning and then drops slowly, as shown in Fig. 13. When the atoms are heated up to a supercritical state with little density decrease, the pressure becomes high. When they start to cool down, the pressure is released and the material layers undergo a rather smooth and homogeneous phase change progress. In this case, the material density keeps decreasing with time so the condition that the term $\frac{d\rho}{dt}$ of Eq. (6) is negative is conserved during the whole process of phase change. It is confirmed by the results

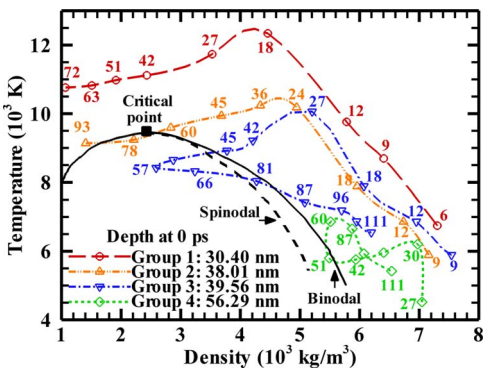

FIG. 13. (Color online) Thermodynamic trajectories of four atom groups. Laser and material parameters are the same as in Fig. 7.

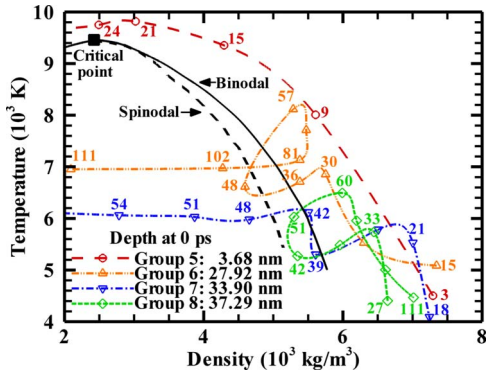

FIG. 14. (Color online) Thermodynamic trajectories of four atom groups. Laser and material parameters are the same as in Fig. 8.

that the plume temperatures shown in Fig. 11 are much higher than the values predicted by the TTM-MD model. Atom group 1 is initially located at a depth around 30 nm, and it reaches a high temperature well beyond the critical point and becomes vapor. Atom groups 2 and 3 are initially located at about the same depth, and the maximum temperatures that atom groups 2 and 3 reach are above the critical point. Their thermal dynamic trajectories are very similar within the first 24 ps, and become different after they start to cool down. Atom group 2 cools down almost adiabatically and reaches the critical point before entering the unstable zone. Atom group 3 cools down with more significant heat diffusion and enters the unstable zone with lower temperature and higher density. Finally, atom group 2 turns into vapor and atom group 3 goes back to the liquid phase. The thermal dynamic trajectories of atom groups 2 and 3 are representative of the phase separation process (around 60 ps). This phenomenon is the so-called critical point phase separation,[63] where the materials that reach the critical point as they cool down will experience the phase separation. Atom group 4 barely touches the binodal line and condenses back to the substrate.

At the low fluence, the material separation mechanism is different from that at the moderate fluence, as shown in Fig. 14. Atom group 5 is located near the surface at time 0, and it succeeds to go over the critical point and expand away. Atom groups 6–8 are located at depths in the range of 27–37 nm at time 0 but their thermal dynamic trajectories and final states are very different. Figures 8 and 10 show that material separation occurs during 48–75 ps. Atom groups do have similar densities and temperatures at 48 ps as shown in Fig. 14. Then from 48 to 57 ps, atom group 7 expands into vapor while atom groups 6 and 8 are compressed into liquid, which is the homogeneous nucleation and phase explosion process. Finally atom group 6 changes to vapor since it has touched the unstable zone inside the spinodal line at 48 ps. During this time period, positive pressure and negative pressure regions occur next to each other in the material layers, and therefore strong tensile stress is formed in several locations and multiple spallations occur at 75 ps (Figs. 8 and 10). For this low fluence case, the material density is not always decreasing with time so the $\frac{d\rho}{dt}$ terms shown in Eqs. (6) and (7) may have a negative sign. Comparing the temperature results predicted by the MD-MC model and the TTM-MD model in Fig. 12, the temperature difference at 42 and 72 ps is now indeed much smaller as compared to the case at 15 ps where the $\frac{d\rho}{dt}$ term is positive. The plume shows another different characteristic, i.e., rapid expansion, as compared with that predicted by the TTM-MD model. And this expansion is not overestimated due to the application of the Morse potential because the Morse potential was used for both of these two models.

In summary, the overall ablation mechanisms at different fluences are very different. At a low fluence (on the order of 0.1 J/cm^2), the tensile stress generated at the interface of positive pressure and negative pressure regions during phase explosion induces multiple spallations. At a moderate fluence (on the order of 1 J/cm^2), the thermal diffusion length is greater and the material structure modification is more homogeneous. On the other hand, the atom thermodynamic trajectory greatly depends on its initial location inside the material. For example, at the low fluence, the atoms initially located near the surface (within several nanometers) can reach a temperature above the critical point and turn into vapor without entering the unstable zone, such as what occurs at the moderate fluence. For another example, at both of these two different fluences, if the material cools down from a supercritical state, the cooling process is nearly adiabatic; otherwise, if the material cools down from a region near the unstable zone, the cooling process is almost isothermal (Figs. 13 and 14).

Comparing with the thermodynamic state change in Si ablated by a laser with similar fluence range and pulse duration in Ref. 21, significant differences of ablation characteristics are found between the semiconductor and the metal. The semiconductor material changes to liquid within 1 ps while the metal (Ni) studied in this paper maintains solid state up to several picoseconds (see Fig. 13; the liquid density of Ni is 7.93×10^3 kg/m^3). Moreover, the metal can be heated up to a temperature much higher than its critical temperature, which is not observed for the semiconductor.

V. CONCLUSION

In this study, it is shown that the electron temperature at the material front surface during USLP irradiation time is lower than what literature suggests, by an MD-MC model including ballistic electron motion and ionization effects. It is also found that even if the interaction between the laser pulse and the ablated material or plasma can be neglected, the hydrodynamic motion and fast density change in the ablated material have a significant effect on the energy transport mechanism. If the ablated material expands in homogeneous state, this hydrodynamic motion leads to a higher temperature of the plume front than previously calculated ones and heat conduction is no longer the same as in the solid state. On the other side, if the ejected material has a form of clusters and undergoes a fast density change, the plume front expands with a greater velocity than previously shown values. The combined MD-MC model developed in the current study provides a feasible way to gain more insight on the fundamental energy transport phenomena during the ultrashort laser ablation.

ACKNOWLEDGMENTS

The authors wish to gratefully acknowledge the financial support provided for this study by the National Science Foundation (Grants No. CMMI-0653578 and No. 0853890-CBET).

APPENDIX: EQUATION OF MOTION FOR ATOM SYSTEM

It is mentioned in Sec. III B that DPD method is used to initialize the system, and thus the initial total momentum of the atom system is 0,

$$\sum (\vec{p}_i) = 0. \tag{A1}$$

Using the definitions of velocity and momentum,

$$\vec{v}_i = \frac{d\vec{r}_i}{dt}, \tag{A2}$$

$$\vec{p}_i = M\vec{v}_i, \quad \vec{p}_i^* = M\vec{v}_i^*, \tag{A3}$$

Eq. (1) can be expressed as

$$\frac{d\vec{p}_i}{dt} = -\nabla_{\vec{r}_i} V - \frac{g}{C_l}\frac{T_l - T_e}{T_l}\vec{p}_i^*. \tag{A4}$$

For a very small time step Δt,

$$\Delta\vec{p}_i = \left(-\nabla_{\vec{r}_i} V\Delta t - \frac{g}{C_l}\frac{T_l - T_e}{T_l}\vec{p}_i^*\right)\Delta t. \tag{A5}$$

For each atom subsystem, a thin material layer where T_e and T_l are defined (as mentioned in Sec. III B), at each time step,

$$\sum_i (\Delta\vec{p}_i) = \left[-\sum_i (\nabla_{\vec{r}_i} V) - \sum_i \left(\frac{g}{C_l}\frac{T_l - T_e}{T_l}\vec{p}_i^*\right)\right]\Delta t. \tag{A6}$$

Since the internal force $-\nabla_{\vec{r}_i} V$ derived from the intermolecular potential V will not change the total momentum of the system, Eq. (A6) can be reformulated as

$$\sum_i (\Delta\vec{p}_i) = -\sum_i \left(\frac{g}{C_l}\frac{T_l - T_e}{T_l}\vec{p}_i^*\right)\Delta t. \tag{A7}$$

Moreover, $\frac{g}{C_l}\frac{T_l - T_e}{T_l}$ is the same for each subdomain so Eq. (A7) can be written as

$$\sum_i (\Delta\vec{p}_i) = -\frac{g}{C_l}\frac{T_l - T_e}{T_l}\sum_i \vec{p}_i^*\Delta t. \tag{A8}$$

Now use the definition of the thermal velocity $\vec{v}_i^* \equiv \vec{v}_i - \vec{v}_c$ and $\vec{p}_i^* = \vec{p}_i - \vec{p}_c$,

$$\sum_i (\Delta\vec{p}_i) = -\frac{g}{C_l}\frac{T_l - T_e}{T_l}\left(\sum_i \vec{p}_i - \sum_i \vec{p}_c\right)\Delta t = 0 \tag{A9}$$

which means that the total momentum change is kept at 0 at each time step, and Eq. (A1) is always satisfied. Therefore, this scheme is momentum conserving.

[1] N. N. Nedialkov, S. E. Imamova, and P. A. Atanasov, J. Phys. D **37**, 638 (2004).
[2] S. I. Anisimov, B. L. Kapeliovich, and T. L. Perel'man, Zh. Eksp. Teor. Fiz. **66**, 776 (1974) [Sov. Phys. JETP **39**, 375 (1975)].
[3] T. Q. Qiu and C. L. Tien, J. Heat Transfer **115**, 835 (1993).
[4] D. Y. Tzou, J. Heat Transfer **117**, 8 (1995).
[5] J. K. Chen and J. E. Beraun, J. Opt. A, Pure Appl. Opt. **5**, 168 (2003).
[6] K. Vestentoft and P. Balling, Appl. Phys. A **84**, 207 (2006).
[7] B. Wu and Y. C. Shin, Appl. Surf. Sci. **253**, 4079 (2007).
[8] M. E. Povarnitsyn, T. E. Itina, K. V. Khishchenko, and P. R. Levashov, Appl. Surf. Sci. **253**, 6343 (2007).
[9] J. K. Chen, D. Y. Tzou, and J. E. Beraun, Int. J. Heat Mass Transfer **49**, 307 (2006).
[10] S. Laville, F. Vidal, T. W. Johnston, O. Barthelemy, M. Chaker, B. LeDrogoff, J. Margot, and M. Sabsabi, Phys. Rev. E **66**, 066415 (2002).
[11] J. P. Colombier, P. Combis, F. Bonneau, R. Le Harzic, and E. Audouard, Phys. Rev. B **71**, 165406 (2005).
[12] Y. V. Afanasiev, B. N. Chichkov, N. N. Demchenko, V. A. Isakov, and I. N. Zavestovskaia, Proc. SPIE **4065**, 349 (2000).
[13] J. T. Larsen and S. M. Lane, J. Quant. Spectrosc. Radiat. Transf. **51**, 179 (1994).
[14] M. E. Povarnitsyn, T. E. Itina, M. Sentis, K. V. Khishchenko, and P. R. Levashov, Phys. Rev. B **75**, 235414 (2007).
[15] J. P. Colombier, P. Combis, A. Rosenfeld, I. V. Hertel, E. Audouard, and R. Stoian, Phys. Rev. B **74**, 224106 (2006).
[16] L. V. Zhigilei and D. S. Ivanov, Appl. Surf. Sci. **248**, 433 (2005).
[17] N. N. Nedialkov, S. E. Imamova, P. A. Atanasov, P. Berger, and F. Dausinger, Appl. Surf. Sci. **247**, 243 (2005).
[18] C. Schäfer, H. M. Urbassek, and L. V. Zhigilei, Phys. Rev. B **66**, 115404 (2002).
[19] C. Cheng and X. Xu, Phys. Rev. B **72**, 165415 (2005).
[20] B. C. Stuart, M. D. Feit, S. Herman, A. M. Rubenchik, B. W. Shore, and M. D. Perry, Phys. Rev. B **53**, 1749 (1996).
[21] P. Lorazo, L. J. Lewis, and M. Meunier, Phys. Rev. B **73**, 134108 (2006).
[22] B. Rethfeld, A. Kaiser, M. Vicanek, and G. Simon, Phys. Rev. B **65**, 214303 (2002).
[23] L. Romanó and V. Dallacasa, J. Phys.: Condens. Matter **2**, 4717 (1990).
[24] U. Mizutani, *Introduction to the Electron Theory of Metals* (Cambridge University Press, Cambridge, 2001).
[25] Y. B. Zel'dovich and Y. P. Raizer, *Physics of Shock Waves and High-Temperature Hydrodynamic Phenonmena* (Dover, New York, 2002).
[26] S. S. Wellershoff, J. Hohlfeld, J. Güdde, and E. Matthias, Appl. Phys. A [Suppl.] **69**, S99 (1999).
[27] S. C. Meepagala and M. C. Baykul, Phys. Rev. B **50**, 13786 (1994).

[28] C. O. Park, H. W. Lee, T. D. Lee, and J. K. Kim, Appl. Phys. Lett. **52**, 368 (1988).
[29] Y. L. Shao, V. Zafiropulos, A. P. Georgiadis, and C. Fotakis, Z. Phys. D **21**, 299 (1991).
[30] B. Witzel, C. J. G. J. Uiterwaal, H. Schröder, D. Charalambidis, and K.-L. Kompa, Phys. Rev. A **58**, 3836 (1998).
[31] R. Mibuka, S. Hassaballa, K. Uchino, H. Yurimoto, R. Todokoro, K. Kumondai, and M. Ishihara, Appl. Surf. Sci. **255**, 1595 (2008).
[32] D. V. Fisher, Z. Henis, S. Eliezer, and J. Meyer-ter-vehn, Laser Part. Beams **24**, 81 (2006).
[33] E. K. Asibu, Jr., *Principles of Laser Materials Processing* (Wiley, New York, 2009).
[34] R. A. Snavely, M. H. Key, S. P. Hatchett, T. E. Cowan, M. Roth, T. W. Phillips, M. A. Stoyer, E. A. Henry, T. C. Sangster, M. S. Singh, S. C. Wilks, A. MacKinnon, A. Offenberger, D. M. Pennington, K. Yasuike, A. B. Langdon, B. F. Lasinski, J. Johnson, M. D. Perry, and E. M. Campbell, Phys. Rev. Lett. **85**, 2945 (2000).
[35] E. Leveugle, D. S. Ivanov, and L. V. Zhigilei, Appl. Phys. A **79**, 1643 (2004).
[36] Y. Gan and J. K. Chen, Appl. Phys. Lett. **94**, 201116 (2009).
[37] V. V. Zhakhovskii, N. A. Inogamov, and K. Nishihara, J. Phys.: Conf. Ser. **112**, 042080 (2008).
[38] S. I. Anisimov, N. A. Inogamov, Y. V. Petrov, V. A. Khokhlov, V. V. Zhakhovskii, K. Nishihara, M. B. Agranat, S. I. Ashitkov, and P. S. Komarov, Appl. Phys. A **92**, 797 (2008).
[39] J. K. Chen, J. E. Beraun, L. E. Grimes, and D. Y. Tzou, Int. J. Solids Struct. **39**, 3199 (2002).
[40] S. E. Imamova, P. A. Atanasov, N. N. Nedialkov, F. Dausinger, and P. Berger, Nucl. Instrum. Methods Phys. Res. B **227**, 490 (2005).
[41] A. I. Karasevskii and V. V. Lubashenko, Phys. Status Solidi B **241**, 1274 (2004).
[42] K.-N. Chiang, C.-Y. Chou, C.-J. Wu, and C.-A. Yuan, Appl. Phys. Lett. **88**, 171904 (2006).
[43] G. Besold, I. Vattulainen, M. Karttunen, and J. M. Polson, Phys. Rev. E **62**, R7611 (2000).
[44] D. S. Ivanov and L. V. Zhigilei, Phys. Rev. B **68**, 064114 (2003).
[45] D. Frenkel and B. Smit, *Understanding Molecular Simulation: From Algorithms to Applications* (Academic Press, San Diego, CA, 2002).
[46] D. Vasileska and S. M. Goodnick, *Computational Electronics* (Morgan and Claypool, San Rafael, CA, 2006).
[47] J. M. Fernández-Varea, J. D. Martínez, and F. Salvat, J. Phys. D **24**, 814 (1991).
[48] X. Guo, Z. Fang, A. S. Kheifets, S. A. Canney, M. Vos, I. E. McCarthy, and E. Weigold, Phys. Rev. B **57**, 6333 (1998).
[49] K. Nanbu, IEEE Trans. Plasma Sci. **28**, 971 (2000).
[50] Y. Weng and M. J. Kushner, Phys. Rev. A **42**, 6192 (1990).
[51] M. A. Tas, E. M. van Veldhuizen, and W. R. Rutgers, J. Phys. D **30**, 1636 (1997).
[52] O. M. Ivanenko and K. V. Mitsen, Physica C **282-287**, 1179 (1997).
[53] A. H. MacDonald, Phys. Rev. Lett. **44**, 489 (1980).
[54] C. Momma, B. N. Chichkov, S. Nolte, F. von Alvensleben, A. Tünnermann, and H. Welling, Opt. Commun. **129**, 134 (1996).
[55] A. V. Lugovskoy and I. Bray, J. Phys. D **31**, L78 (1998).
[56] W. Lotz, Z. Phys. **232**, 101 (1970).
[57] S. Preuss, A. Demchuk, and M. Stuke, Appl. Phys. A **61**, 33 (1995).
[58] S. Nolte, C. Momma, H. Jacobs, A. Tünnermann, B. N. Chichlov, B. Wellegehausen, and H. Welling, J. Opt. Soc. Am. B **14**, 2716 (1997).
[59] C. Porneala and D. A. Willis, Int. J. Heat Mass Transfer **49**, 1928 (2006).
[60] J. M. Soler, M. R. Beltrán, K. Michaelian, I. L. Garzón, P. Ordejón, D. Sánchez-Portal, and E. Artacho, Phys. Rev. B **61**, 5771 (2000).
[61] R. M. More, K. H. Warren, D. A. Young, and G. B. Zimmerman, Phys. Fluids **31**, 3059 (1988).
[62] B. Chimier and V. T. Tikhonchuk, Phys. Rev. B **79**, 184107 (2009).
[63] F. Vidal, T. W. Johnston, S. Laville, O. Barthélemy, M. Chaker, B. Le Drogoff, J. Margot, and M. Sabsabi, Phys. Rev. Lett. **86**, 2573 (2001).